AIAA SciTech
4-8 January 2016, San Diego, California, USA
54th AIAA Aerospace Sciences Meeting

Adjoint-based Mesh Adaptation for the 3D Navier-Stokes Equations with the High-order CPR Method

Lei Shi* and Z.J. Wang †
Department of Aerospace Engineering, University of Kansas, Lawrence, KS, 66045

The objective of the present work is to extend the adjoint-based error estimate and the adaptive mesh refinement algorithm of the high-order CPR method to the 3D Navier-Stokes equations. A dual-consistent high-order correction procedure via reconstruction method is utilized to obtain the adjoint solution and derive the output-based local error indicator. Several inviscid and viscous flow cases are utilized to evaluate the effectiveness of the present adaptive method. Numerical tests show that significant savings in the number of DOFs can be achieved through the present method.

I. Introduction

With continuous progresses in numerical methods and computer hardware over the past several decades, Computational Fluid Dynamics (CFD) is now used routinely as a powerful tool in the design of aircraft. As it is still too expensive to obtain mesh-independent simulations in 3D, design computations still rely heavily on the experience of CFD users to generate results of "engineering accuracy". In this paper, we developed a robust and efficient CFD framework for the 3D Navier-Stokes equations that can provide engineering accuracy with little user interference by using automated mesh adaptation with a reliable error estimation.

Current production CFD codes used in the aerospace industry are usually second order accurate. High-order methods have the potential to achieve higher accuracy at lower cost than lower order methods. This potential has been demonstrated conclusively for smooth problems in the recent several International Workshops on High-Order Methods [41]. For non-smooth problems, solution based hp-adaptations offer the best promise. Adaptive methods have the capability of dynamically distributing computing resources to desired areas to achieve required accuracy with minimal costs [4, 5, 16, 27]. It can ensure the reliability and increase the robustness of the high-order methods. Therefore, adaptive high-order methods have received considerable attentions in the high-order CFD community. [7, 8, 14, 35–37, 45]. The effectiveness of adaptive methods highly depends on the accuracy of the error estimation and the adaptation criteria. Adjoint-based methods can capture the propagation effects inherent in hyperbolic equations and have been shown very effective in driving an hp-adaptation procedure to obtain a very accurate functional output [9, 10]. In the present work, to minimize the output error, the mesh refinement is driven by an automated output-based error estimation method using a dual-consistent CPR formulation.

The rest of the paper is organized as follow: in Section 2, we briefly review the high-order CPR method. The adjoint-based error estimation and mesh adaptation is presented in Section 3. In Section 4, several numerical tests are performed to assess the effectiveness of the present adaptive method. Finally, conclusions and some possible future work are given in Section 5.

II. Review of the Correction Procedure via Reconstruction Method

Right now, a variety of high order methods have been developed. Refer to several books [15, 21, 40] and reviews [6, 39] for the state-of-the-art and recent progress in the development of such methods. Currently, one of the most widely used high-order methods for the compressible Navier-Stokes equations on unstructured

*Post-doctoral researcher, Department of Aerospace Engineering, 2120 Learned Hall, Lawrence, KS 66045, AIAA Member.
†Spahr Professor and Chair, Department of Aerospace Engineering, 2120 Learned Hall, Lawrence, KS 66045, Associate Fellow of AIAA.

grids is the discontinuous Galerkin (DG) method. In order to improve the efficiency of the DG method, high-order methods in the differential form have been developed. The correction procedure via reconstruction (CPR) method is a nodal differential formulation first proposed by Huynh in the framework of the flux reconstruction (FR) [17]. This method is easy to understand, efficient to implement and can recover several known methods such as the DG method, the spectral volume method (SV) [26, 38, 44] and the spectral difference methods (SD) [22, 25, 26, 28, 34]. The framework was applied to solve diffusion problems using quadrilateral meshes in [18]. Wang and Gao extended the FR idea to 2D triangular [42] and mixed meshes with the lifting collocation penalty (LCP) formulation. In Ref. [32], CPR was further extended to 3D hybrid meshes. Some recent developments of the CPR method can be found in Ref. [1, 3, 12, 13, 19, 20, 24, 30, 43].

The CPR method can be derived by transforming a weighted residual method or variational forms into a differential one. Consider a hyperbolic conservation law

$$\frac{\partial Q}{\partial t} + \nabla \cdot \vec{F}(Q) = 0, \tag{1}$$

with proper initial and boundary conditions, where Q is the state vector, and $\vec{F} = (F, G)$ is the flux vector. Assume that the computational domain Ω is discretized into N non-overlapping triangular elements $\{V_i\}_{i=1}^{N}$. Let W be an arbitrary weighting function or testing function. The weighted residual formulation of Eq.1 on elementV_i can be expressed as

$$\int_{V_i} \left(\frac{\partial Q}{\partial t} + \nabla \cdot \vec{F}(Q) \right) W \mathrm{d}\Omega = 0. \tag{2}$$

Let Q_i be an approximate solution to the analytical solution Q on V_i. On each element, the solution belongs to the space of polynomials of degree n or less, i.e., $Q_i \in P^k(V_i)$. After applying integration by parts twice to the flux divergence and replacing the normal flux term with a common Riemann flux F^n_{com} in the above equation, we get

$$\int_{V_i} \frac{\partial Q_i}{\partial t} W \mathrm{d}\Omega + \int_{V_i} W \nabla \cdot \vec{F}(Q_i) \mathrm{d}\Omega + \int_{\partial V_i} W \left[F^n_{com} - F^n(Q_i) \right] \mathrm{d}S = 0. \tag{3}$$

Here the common Riemann flux F^n_{com} is defined as

$$F^n_{com} = F^n_{com}(Q_i, Q_{i+}, \vec{n}), \tag{4}$$

where Q_{i+} denotes the solution outside the current element V_i. And the normal flux $F^n(Q_i)$ at the boundaries is

$$F^n(Q_i) = \vec{F}(Q_i) \cdot \vec{n}. \tag{5}$$

In order to eliminate the test function, the boundary integral above is cast as a volume integral via the introduction of a "correction field" on V_i, $\delta_i \in P^k(V_i)$,

$$\int_{V_i} W \delta_i \mathrm{d}\Omega = \int_{\partial V_i} W [F^n] \mathrm{d}S, \tag{6}$$

where $[F^n] = F^n_{com} - F^n(Q_i)$ is the normal flux difference. Substituting Eq.6 into Eq.3, we obtain

$$\int_{V_i} \left(\frac{\partial Q_i}{\partial t} + \nabla \cdot \vec{F}(Q_i) + \delta_i \right) W \mathrm{d}\Omega = 0. \tag{7}$$

If the flux vector is a linear function of the state variable, then $\nabla \cdot \vec{F}(Q_i) \in P^k$. In this case, the terms inside the square bracket are all elements of P^n. Because the test space is selected to ensure a unique solution, Eq.7 is equivalent to

$$\frac{\partial Q_i}{\partial t} + \nabla \cdot \vec{F}(Q_i) + \delta_i = 0. \tag{8}$$

For nonlinear conservation laws, $\nabla \cdot \vec{F}(Q_i)$ is usually not an element of P^k. As a result, Eq.7 cannot be reduced to Eq.8. In this case, the most obviously choice is to project $\nabla \cdot \vec{F}(Q_i)$ into P^k. Denote $\Pi\big(\nabla \cdot \vec{F}(Q_i)\big)$ as a projection of $\nabla \cdot \vec{F}(Q_i)$ to P^k. One choice is

$$\int_{V_i} \Pi\big(\nabla \cdot \vec{F}(Q_i)\big) W \mathrm{d}\Omega = \int_{V_i} \nabla \cdot \vec{F}(Q_i) W \mathrm{d}\Omega. \tag{9}$$

Then Eq.7 reduces to

$$\frac{\partial Q_i}{\partial t} + \Pi\big(\nabla \cdot \vec{F}(Q_i)\big) + \delta_i = 0. \tag{10}$$

Next, let the DOFs be the solutions at a set of solution points (SPs) $\{\vec{r}_{i,j}\}$ (j varies from 1 to $K = (n+1)(n+2)/2$). Then Eq.10 holds true at the SPs, i.e.,

$$\frac{\partial Q_{i,j}}{\partial t} + \Pi_j\big(\nabla \cdot \vec{F}(Q_i)\big) + \delta_{i,j} = 0, \tag{11}$$

where $\Pi_j\big(\nabla \cdot \vec{F}(Q_i)\big)$ denotes the values of $\Pi\big(\nabla \cdot \vec{F}(Q_i)\big)$ at SP j. The efficiency of the CPR approach hinges on how the correction field δ_i and the projection $\Pi\big(\nabla \cdot \vec{F}(Q_i)\big)$ are computed. Two approaches can be used to compute the projection of the flux divergence as detailed in Ref. [42]. For a simple notation, the projection operator Π is ignored for the rest of the paper.

To compute δ_i, we define n+1 points named flux points (FPs) along each interface, where the normal flux differences are computed. We approximate (for nonlinear conservation laws) the normal flux difference $[F^n]$ with a degree n interpolation polynomial along each interface,

$$[F^n]_f \approx \mathbf{I}_k [F^n]_f \equiv \sum_l [F^n]_{f,l} L_l^{FP}, \tag{12}$$

where f is a face (or edge in 2D) index, and l is the FP index, and L_l^{FP} is the Lagrange interpolation polynomial based on the FPs in a local interface coordinate. For linear triangles with straight edges, once the solution points and flux points are chosen, the correction at the SPs can be written as

$$\delta_{i,j} = \frac{1}{|V_i|} \sum_{f \in \partial V_i} \sum_l \alpha_{j,f,l} [F^n]_{f,l} S_f, \tag{13}$$

where $\alpha_{j,f,l}$ are lifting constants independent of the solution variables, S_f is the face area, $|V_i|$ is the volume of V_i. The details of how to compute the lifting constants$\alpha_{j,f,l}$ can be found in Ref. [42].

In 1D, a continuous flux polynomial $\hat{F}$ which is equal to the common flux at the interfaces can be reconstructed using a piece-wise analytic flux polynomial $F_i(x) = \Pi(F(Q_i))$ and a correction term $\sigma_i(x)$. In order to achieve an efficient implementation, all elements are transformed from the physical domain x into a standard element in the computational domain $\xi \in [-1, 1]$ by

$$x = x_{i-1/2} + \frac{h_i}{2}(\xi + 1), \tag{14}$$

where h_i is the length of cell i and $x_{i-\frac{1}{2}}$ is the x coordinate of cell i's left boundary. On cell i, the reconstructed continuous flux polynomial $\hat{F}$ can be written as

$$\hat{F}_i(\xi) = F_i(\xi) + \sigma_i(\xi). \tag{15}$$

According to Ref.[17], $\sigma_i(\xi)$ should approximate the zero function and satisfy the following equation

$$\sigma_i(\xi) = [F_{i-1/2}^{com} - F_i(-1)] g_L(\xi) + [F_{i+1/2}^{com} - F_i(1)] g_R(\xi). \tag{16}$$

Here, $g_L(\xi)$ and $g_R(\xi)$ are both degree $k+1$ polynomials called correction functions with the properties

$$g_L(-1) = 1, \quad g_L(1) = 0, \quad g_R(-1) = 0, \quad g_R(1) = 1. \tag{17}$$

Then the CPR method for the 1D conservation law can be expressed as

$$\frac{\partial Q_{i,j}}{\partial t} + \frac{\partial F_i(\xi)}{\partial \xi} \frac{2}{h_i} + \frac{2}{h_i} [F_{i-1/2}^{com} - F_i(-1)] g_L'(\xi_{i,j}) + \frac{2}{h_i} [F_{i+1/2}^{com} - F_i(x_{i+1/2})] g_R'(\xi_{i,j}) = 0. \tag{18}$$

A series of correction functions with different accuracy and stability properties were developed in Ref. [17]. If the correction function g is chosen as right Radau polynomials, the DG method is recovered from the CPR scheme. For the sake of simplicity, the projection operator Π is omitted in the rest of the paper. The CPR method for the hexahedral element is a tensor product of the 1D formulation in each axis.

III. Adjoint-based Error Estimation and H-adaptation

Adjoint-based error estimation relates a specific functional output directly to the local residuals by the adjoint solution, which can be used to construct a very effective error indicator to drive an adaptive procedure toward any engineering output. Let Q_h denotes an approximate solution to the analytical solution Q. The difference between them can be interpreted as a solution perturbation $\delta Q = Q - Q_h$. The output error defined as $\delta\mathcal{J} = \mathcal{J}(Q_h) - \mathcal{J}(Q)$ can be estimated by the adjoint weighted residual method

$$\delta\mathcal{J} \approx -\int_\Omega \psi(\mathcal{N}(Q_h) - \mathcal{N}(\mathrm{Q}))\mathrm{d}\Omega = -\int_\Omega \psi\mathcal{N}(Q_h)\mathrm{d}\Omega. \tag{19}$$

Since the CPR method is not in a variational form, the discrete adjoint formulation for the CPR method utilizes an explicitly defined variational form to obtain the dual-consistent adjoint solution. Assume the adjoint solution belongs to the same space of the primal solution, the adjoint variable ψ_i of cell i can be approximated using the Lagrange basis L_j

$$\psi_i = \sum_j L_j \psi_{i,j}. \tag{20}$$

The discrete adjoint equation for the CPR method reads

$$-\sum_i \sum_j \frac{\partial r_{i,j}}{\partial Q_l}\omega_j |J_{i,j}|\psi_{i,j} = \frac{\partial \mathcal{J}}{\partial Q_l}, \tag{21}$$

where $r_{i,j}$ is a pointwise residual defined on each solution point j of cell i arising from a CPR scheme and ω_j and $|J_{i,j}|$ are the quadrature weight and the element Jacobian at the solution point. More detailed discussion about the dual-consistency of the CPR method can be found in Ref. [29].

Based on Eq. 19, the output error estimate can be expressed as

$$\delta\mathcal{J} \approx -\sum_i \sum_j r_{i,j}(Q_h)\omega_j |J_{i,j}|\psi_{i,j}. \tag{22}$$

Also, we can define a corrected output using the functional error estimate

$$\mathcal{J}_{corr} \equiv \mathcal{J}(Q_h) + \delta\mathcal{J}. \tag{23}$$

From the Eq. 19, the output error can be estimated by performing a quadrature rule as

$$\delta\mathcal{J}_h(Q_h) \approx -\sum_i \sum_j \omega_j |J_{i,j}|\psi_{i,j} r_{i,j}(Q_h^H). \tag{24}$$

The continuous adjoint solution ψ is approximated by solving ψ_h on the finner space through enriching the degree of the solution polynomial. The finer solution Q_h is obtained by performing several steps of GMRES relaxation after prolongating from the coarse solution Q_H

$$Q_h^H = I_h^H Q_H \tag{25}$$

with an injection operator I_h^H. The adjoint-based local error indicator η_i used in this paper is defined by taking an absolution value of the elemental output error contribution

$$\eta_i = |\sum_j \omega_j |J_{i,j}| \left(\psi_h - I_h^H \psi_H\right)_{i,j} r_{i,j}(Q_h^H)|. \tag{26}$$

Here, to achieve a better estimates, the adjoint defect between the coarse level and fine level $\psi_h - I_h^H\psi_H$ is used. For systems of equation, the local error indicators are formed by summing together every component's contribution to the functional error estimate.

The error indicators defined above are used to drive a fixed-fraction h-adaptation. In this approach, a certain fraction f of the current elements with the largest local error indicators η are marked for h-refinements. Figure 1 shows the procedure of the adjoint-based h-adaptation for the CPR method.

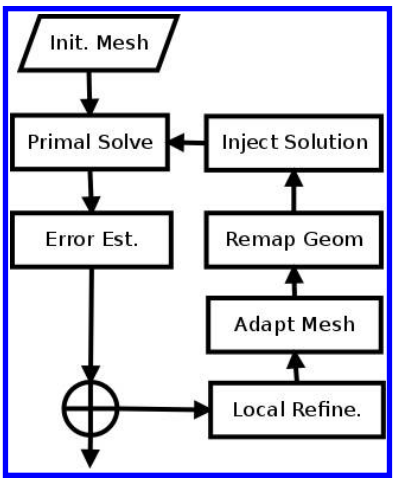

Figure 1: The procedure of the adjoint-based h-adaptation.

Mesh refinement is performed in the original element's polynomial space using the reference coordinates. So the refined elements inherit the same geometry approximation order. However, for elements on the geometry boundaries, the newly generated vertex on the boundary edge may not be exactly on the real geometry. An extra remapping process is employed to snap the boundary points to the truth geometry during each adaptation level.

III.A. Non-conforming Interface

Non-conforming interfaces between cells with different h or p levels are created during the adaptations. In order to ensure the solution smoothness, only one level difference of h-refinement between neighboring cells are allowed Figure 2. Special treatment is required when computing the common numerical flux on those non-conforming interfaces with hanging nodes. The "mortar" element method developed by Kopriv [23] is used here. Basically, a L_2 projection is used to preserve the global conservation and maintain the accuracy. For a non-conforming interface, a "mortar" face is introduced to link the unmatched elements, whose space are always chosen as the higher h or p space of the two sides. First, the solution from the left and right sides of the face are prolongated to the mortar surface by a simple interpolation process (see Figure 3a on the following page). Then, the common flux are computed by solving the Riemann problem on the mortar surface. The last step is to project the common flux on the mortar surface back to the original space. Here, the standard L_2 projection is utilized to preserve the average.

Let's take a 2D non-conforming h-surface as a example to illustrate the projection procedure. Here, one mortar element links one coarse surface denoted by σ on one side and multiple finer surfaces denoted by σ_k on the other side (see Figure 3b on the next page). Denote the DOFs on the coarse surface σ by Q_j and its basis function by ϕ_j, $j = 1, ..., K$, where K is the number of FPs on that surface. In addition, let $\hat{Q}_{k,j}$ and $\hat{\phi}_{k,j}$ stand for the DOFs and its basis on the k_{th} finer surface σ_k, where $j = 1, ..., K$. The standard L_2 projection from the finer space to the coarse space can be written as,

$$\sum_{k=1}^{nk}\sum_{,j=1}^{K}(\int_{\sigma_k}\phi_i\hat{\phi}_{k,j}d\xi d\eta)\hat{Q}_{k,j} = \sum_{j=1}^{K}(\int_{\sigma}\phi_i\phi_j d\xi d\eta)Q_j, \tag{27}$$

where nk stands for the number of the finer surface connected to the mortar element, which is equal to 2 in 2D and 4 in 3D. Note that the integral on the RHS is the mass matrix evaluated on the coarse space. If the standard Gauss quadrature points are used as the FPs, the shape function ϕ_i defined on each FP is orthogonal to each other, which leads to

$$\int_{\sigma}\phi_i\phi_j d\xi d\eta = \delta_{i,j}, \tag{28}$$

where

$$\delta_{i,j} = \begin{cases} 0 & i \neq j \\ 1 & i = j \end{cases} \tag{29}$$

is the Kronecker delta function.

Thus, the DOFs on the coarse space can be obtained by

$$\sum_{k=1}^{nk} \sum_{,j=1}^{K} \mathbf{R}_{i,(k,j)} \hat{Q}_{k,j} = Q_i. \tag{30}$$

Note $\mathbf{R}_{i,(k,j)}$ stands for the restriction matrix defined as

$$\mathbf{R}_{i,(k,j)} = \int_{\sigma_k} \phi_i \hat{\phi}_{k,j} d\xi d\eta, \tag{31}$$

which can be computed and stored in the preprocessing stage. Similar procedures can be obtained for the non-conforming p-interface. Detailed discussion of the "mortar" method can be found in Ref. [11, 22].

To assess the accuracy of the mortar method, the 3D isentropic vortex propagation case investigated in Ref. [31] is simulated on a hexahedral grid with hanging nodes. The hanging nodes are generated randomly on the initial mesh across the whole computational domain. Then, the uniform h-refinement study is performed for the CPR method with $k = 1 \sim 5$. Figure 4a shows the density contours with $k = 1$ to $k = 5$ on the coarsest mesh. The solution is quite smooth, which indicates that the flow field is not degenerated by the non-conforming surfaces. Figure displays the L2 density error. The optimal orders of accuracy are obtained for the CPR method with the mortar element.

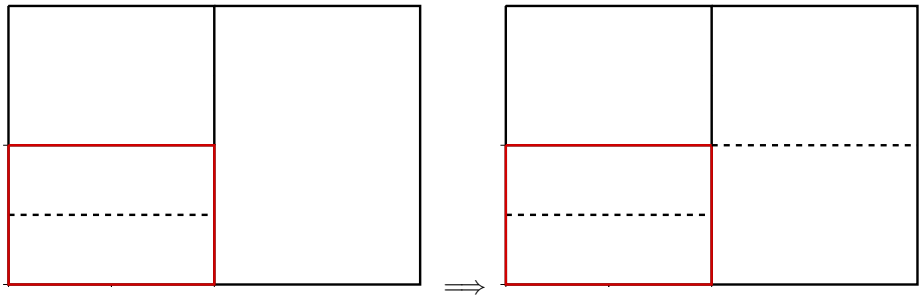

Figure 2: Hanging nodes with the one level difference restriction.

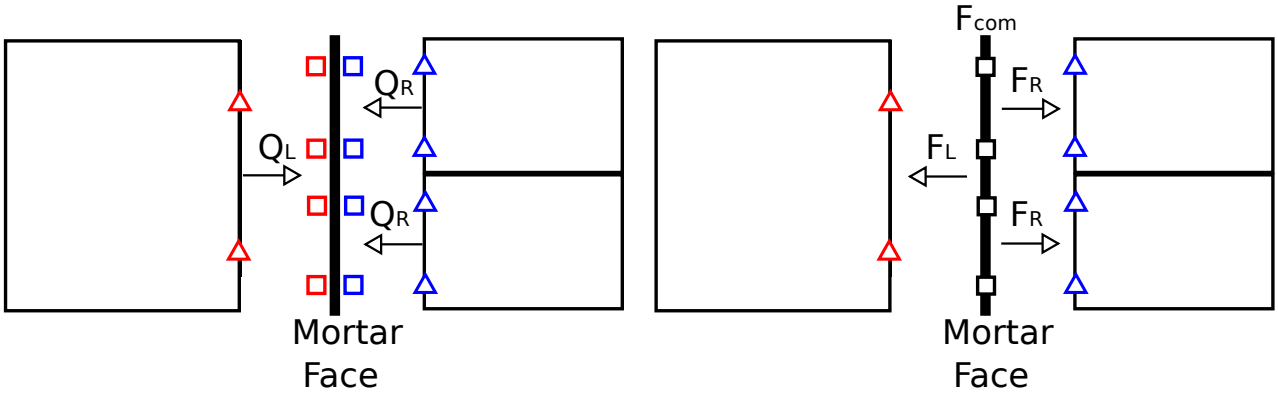

(a) Solution prolongation

(b) Common flux restriction

Figure 3: The mortar face method for non-conforming faces ($k = 1$, △: FPs, □: DOFs on the mortar face).

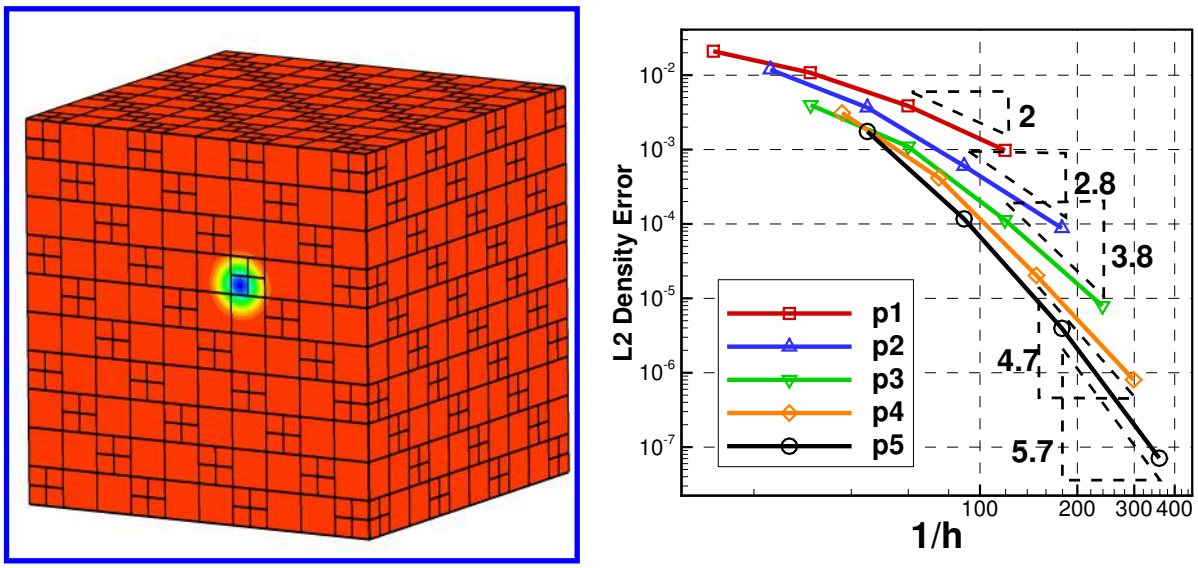

(a) Density contours, k=5 on the initial mesh

(b) L_2 density error vs h

Figure 4: Vortex propagation case with hanging nodes.

IV. Numerical Results

IV.A. Inviscid Flow over a Sphere

In this case, we consider subsonic inviscid flow over a sphere. The p3 hexahedral mesh is used for this simulation. Figure 5 shows the outline of the computational domain and the initial surface mesh on the sphere. The inflow Mach number is set to be 0.3 with an angle of attack $\alpha = 0°$.

First, to demonstrate the super convergence of the output using a dual-consistent CPR formulation, a uniform refinement study is performed. As shown in Figure 6, a super convergence of $2k + 1$ is obtained for the C_D error with $k = 1$ and $k = 2$. For the adaptive simulation, a relative coarse mesh which has 480 p3 hexahedral elements is used as the initial grid and the 3^{rd} order CPR scheme with the Gauss points as the SPs/FPs and the LP approach is tested. The adaptation is driven by the adjoint-based error indicator with drag coefficients as the output of interest. On each adaptation level, 10% of the current elements with the largest error are marked to be refined. The adapted mesh and the Mach contours are shown in Figure 7. Regions around the sphere surface are refined persistently. Figure 8 compares the drag coefficient error of the adaptive simulations with the results from the uniform h-refinements. It is clear to see that the current adaptive method could produce much more efficient error reductions in terms of the number of the DOFs. An effective convergence order of 6 is obtained through the adaptation, which is much faster than the uniform refinements. This preliminary adaptation results demonstrates the effectiveness of the present adaptive method for a 3D problem.

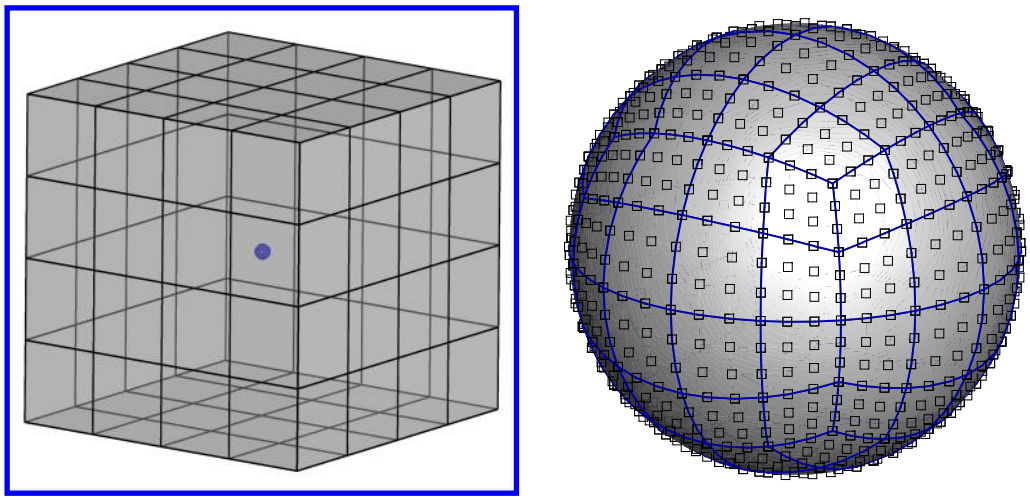

Figure 5: The initial $p3$ curved hexahedral mesh for the inviscid flow over a sphere problem.

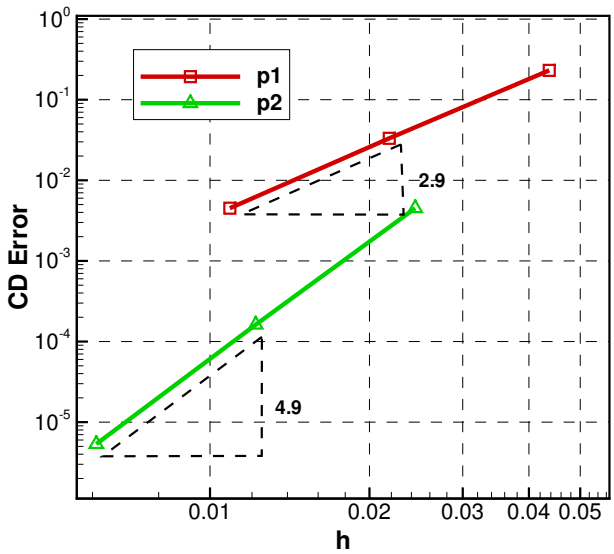

Figure 6: C_D error for the inviscid flow over a sphere problem.

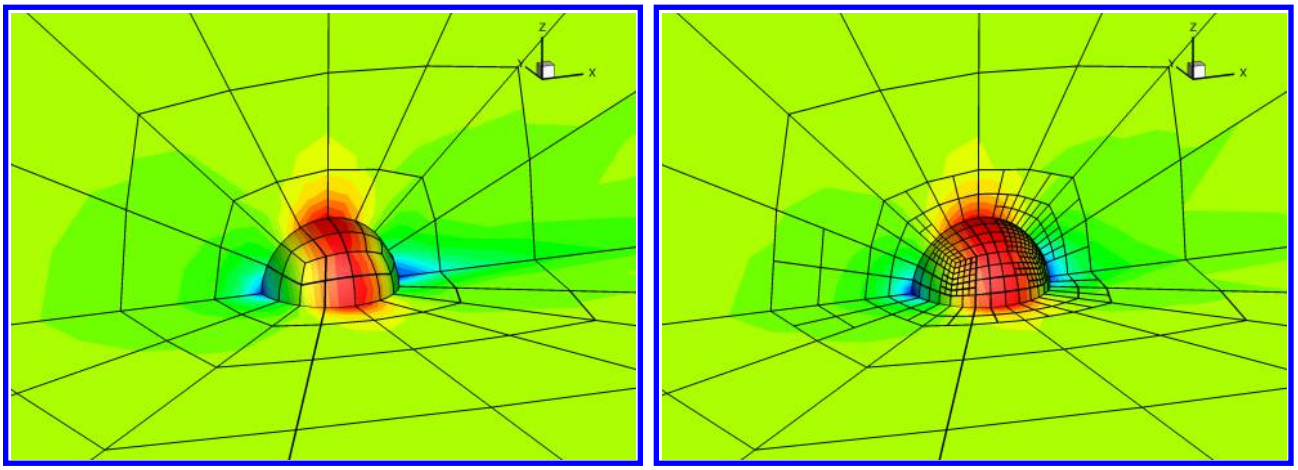

(a) Adaptation level 1 (b) Adaptation level 4

Figure 7: Mach contours on the adapted mesh for the inviscid flow over a sphere at $M_0 = 0.3$, $\alpha = 2°$ $(k = 2)$.

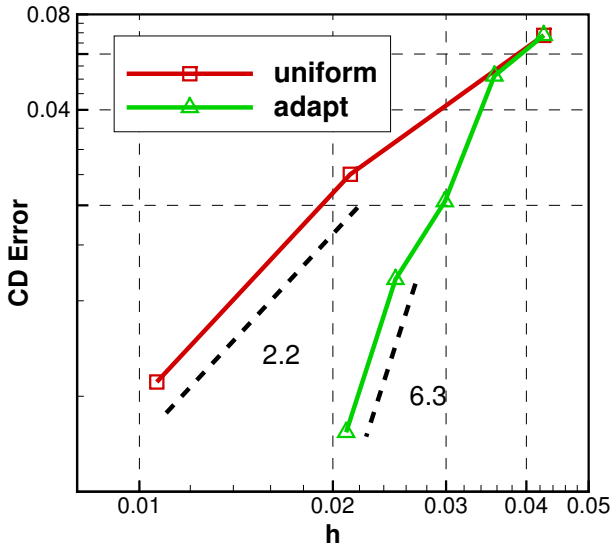

Figure 8: CD errors of the inviscid flow over the sphere at $M_0 = 0.3$, $\alpha = 2°(k = 2)$.

IV.B. Laminar Flow over a Sphere

Next, we consider steady viscous flow over a sphere. The same settings from the Ref. [32, 33] is utilized for the comparison purpose. The Reynolds number based on the sphere diameter is chosen to be 118. The inflow Mach number is 0.2535 with an angle of attack $\alpha = 0°$. The 3^{rd} order CPR scheme with the Gauss points as the SPs/FPs and the LP approach is tested. Figure 9a shows the initial mesh which has 480 p3 hexahedral elements and the corresponding Mach number contours.

The adaptation is driven by the adjoint-based error indicator with drag coefficients as the output of interest. On each adaptation level, 10% of the current elements with the largest error are marked to be refined. The adapted mesh and the Mach contours on each adaptation level are shown in Figure 9. Regions around the sphere surface are refined persistently. The reference $C_D = 1.0162$ is chosen from Ref. [2, 33]. Figure 10 compares the drag coefficient error of the adaptation with the result from the uniform h-refinements.

A super convergence rate of $2k$ is obtained for the uniform h-refinement. The adjoint-based adaptation shows a faster convergence, whose effective order of accuracy is 5.9.

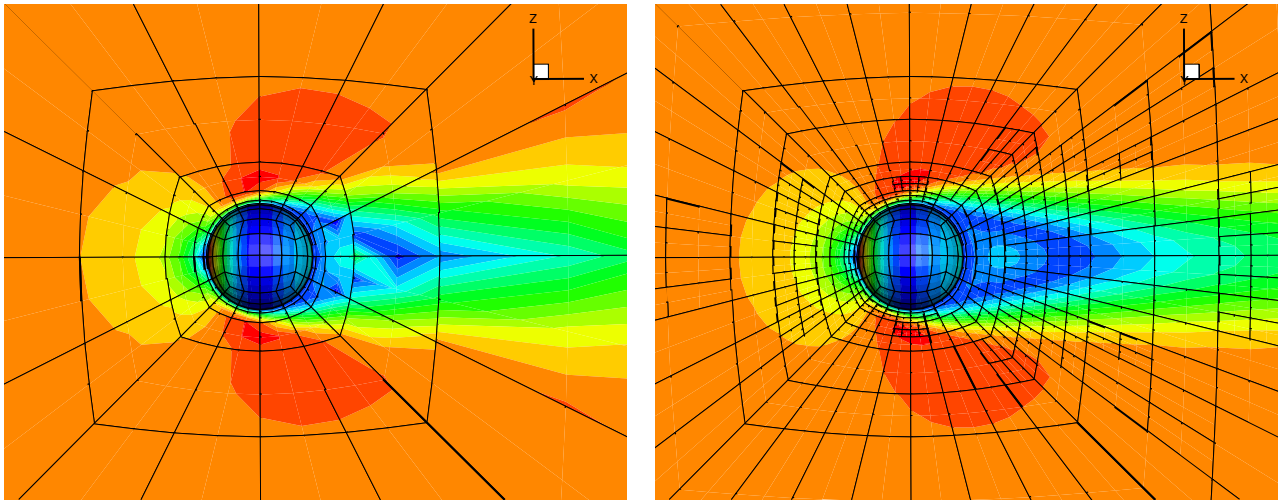

(a) The initial mesh (b) The adapted mesh, level 3

Figure 9: Mach contours and the adapted mesh for the viscous flow over a sphere problem at $M_0 = 0.2535$, $Re = 118$ and $\alpha = 0^\circ$ $(k = 2)$.

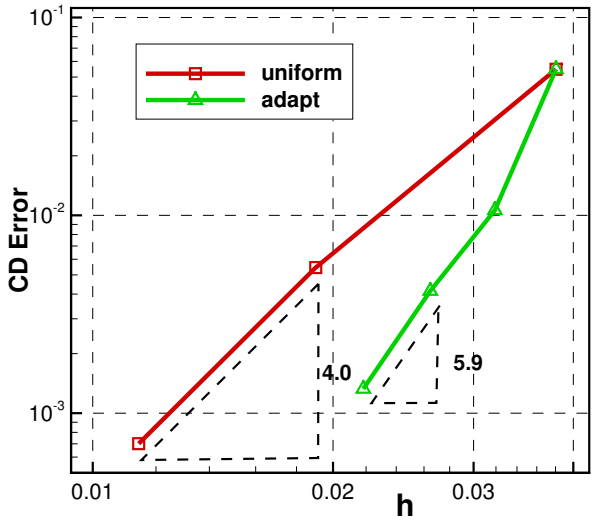

Figure 10: CD errors of the viscous flow over a sphere at $M_0 = 0.2535$, $Re = 118$, $\alpha = 0^\circ$ $(k = 2)$.

IV.C. Laminar Flow over a Delta Wing

In this test case, we consider laminar flow over a delta wing at Mach number $M_0 = 0.3$ with a high angle of attack $\alpha = 12.5^\circ$. This case is a part of the International workshop on high-order methods (HOW) and the EU ADIGMA project. The Reynolds number based on the root chord is 4000. The Prandtl number is set to 0.72 and the constant viscosity is used. The delta wing has a swept sharp leading-edge and a blunt trailing edge. The Mach number contours of the flow around the delta wing at different adaptation stages

are shown in Figure 11. Both of the singularity along the leading edge and the regions around the smooth vortices are targeted to refine. The Mach number distribution is much smoother after several adaptation levels. Figure 12 shows the residual history of the whole adaptation procedure. For each adaptation stage, the residual norm drops 10 order. Figure 13 compares the CD error and the CPU time of the adaptation with the result from the uniform refinements.

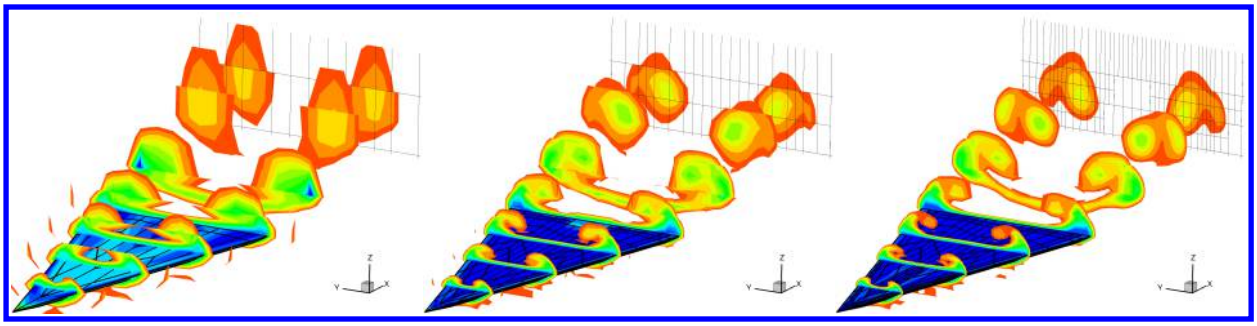

(a) Adaptation level 0 (b) Adaptation level 1 (c) Adaptation level 2

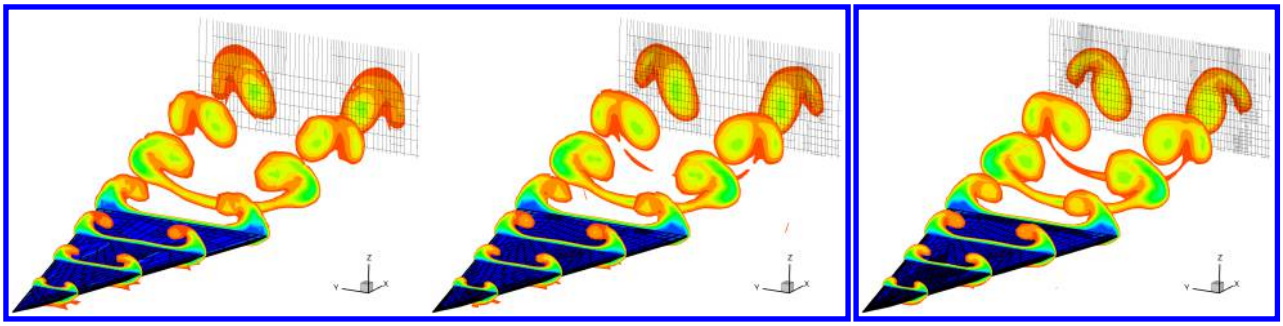

(d) Adaptation level 3 (e) Adaptation level 4 (f) Adaptation level 5

Figure 11: Mach number and the adapted mesh slices on different adaptation stages for the delta wing case.

IV.D. Laminar Flow over an Analytic 3D Body

As the final case, we consider laminar flow over a streamlined analytic 3D body. This test case is a part of the International workshop on high-order methods (HOW) and the EU ADIGMA project. The inflow Mach number is set to 0.5 at an angle of attack $\alpha = 1°$. The Reynolds number is 5000 with adiabatic no-slip wall boundary condition enforced on the body surface. The viscosity is assumed to be a constant and Prandtl number is set to 0.72. The reference area is 0.05 and the reference drag coefficient $C_D = 0.06317$ from the HOW results is used. The coarsest mesh from the HOW website is used as the initial mesh, which consists of 768 p4 curved hexahedral elements. The drag adjoint is used to drive the mesh adaptation procedures. The adapted mesh and the Mach contours are shown in Figure 14b. The refinements are mainly performed around the leading edge and around the body surface. Figure 15 displays the residual history and the C_D error.

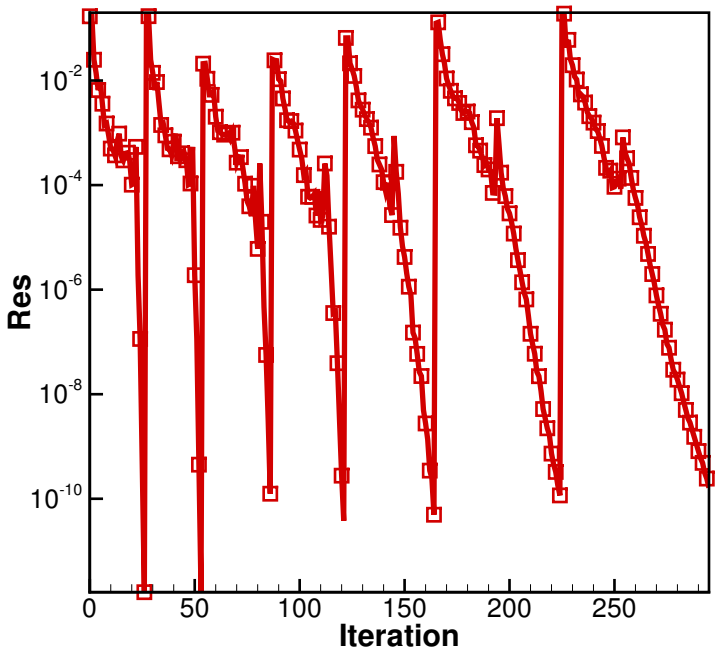

Figure 12: The residual history of the whole adaptation procedure for the delta wing case.

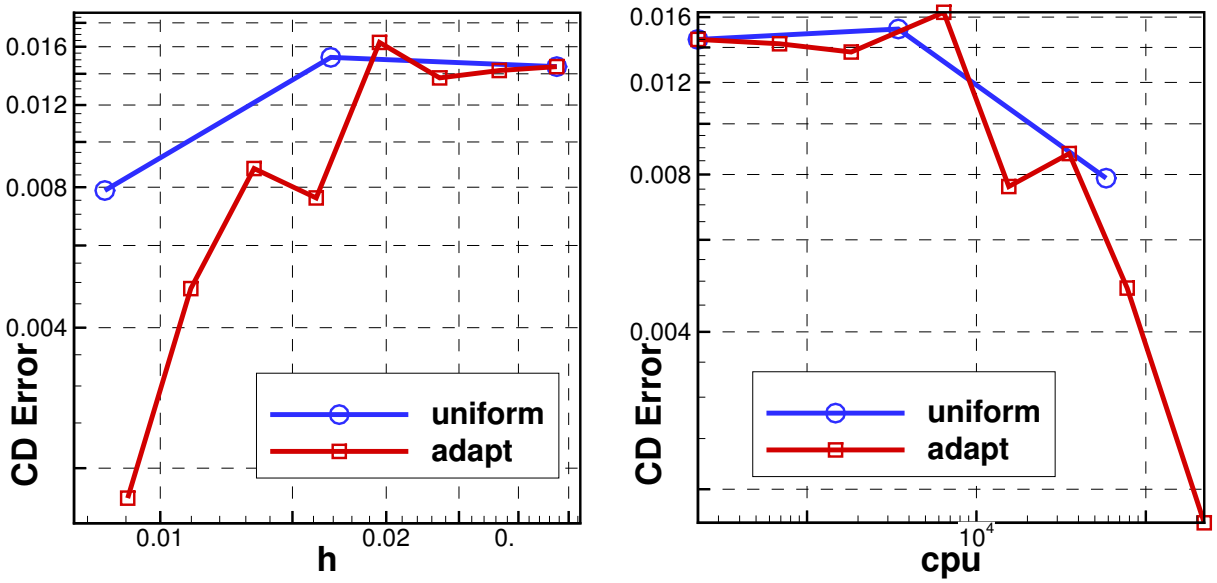

Figure 13: C_D error and the CPU time of the delta wing case.

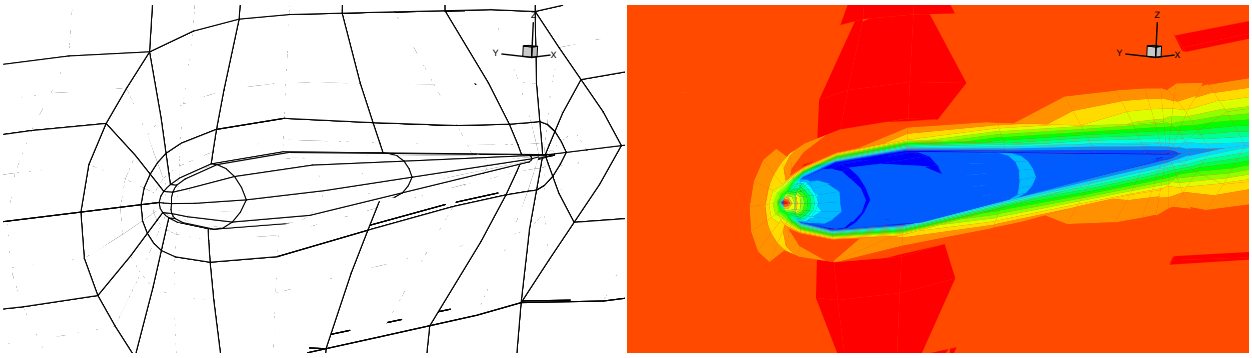

(a) The initial mesh and Mach contours

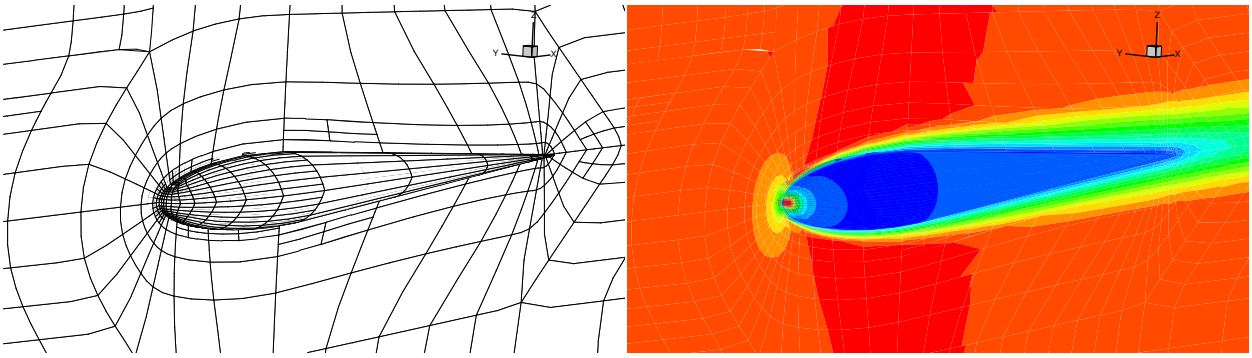

(b) The adapted mesh and Mach contours

Figure 14: Laminar flow over an analytic 3D body at $M_0 = 0.5$, $\alpha = 1°$ and $Re = 5000$.

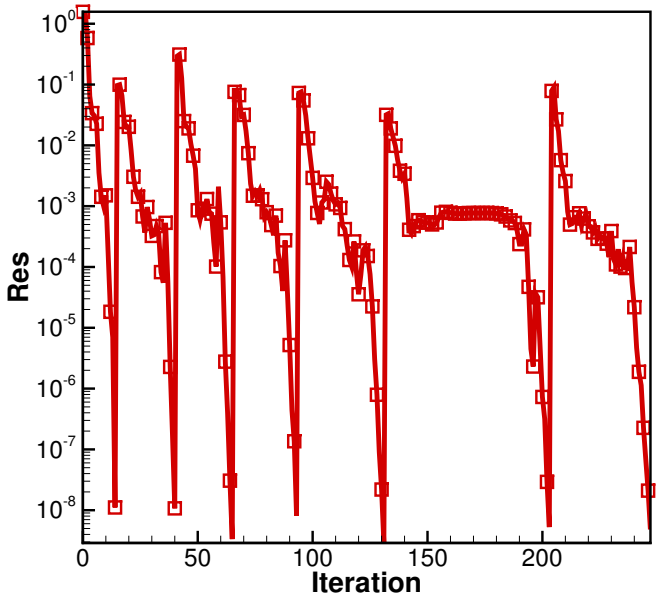

(a) Residual history

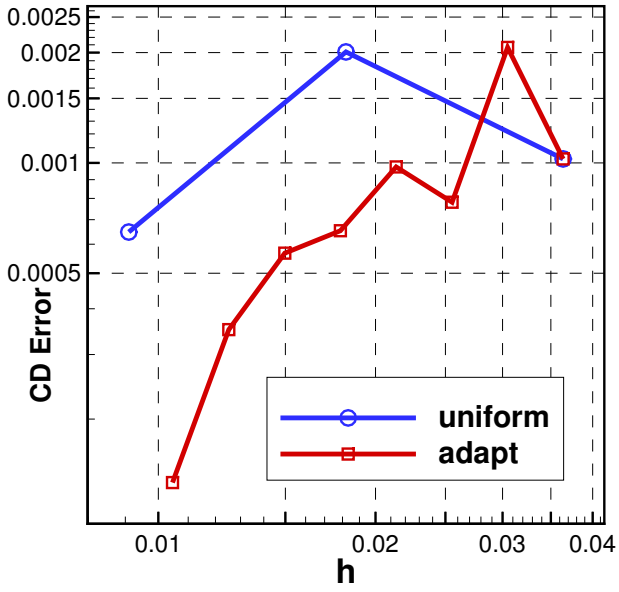

(b) C_D Error

Figure 15: Results of the laminar flow over an analytic 3D body.

V. Conclusions

The objective of the present work is to extend the adjoint-based error estimate and the adaptive mesh refinement algorithm of the high-order CPR method to the 3D Navier-Stokes equations. Several inviscid and viscous flow cases are utilized to evaluate the effectiveness of the present adaptive method. The numerical results show that significant savings in the number of DOFs and the improvement of the solution quality can be achieved through the adjoint-based adaptation. In the future, we will extend the current method to the Reynolds averaged equations and further test it in 3D.

References

[1] Cagnone, J., Vermeire, B., Nadarajah, S., 2013. A p-adaptive LCP formulation for the compressible Navier-Stokes equations. Journal of Computational Physics 233, 324 – 338.

[2] Castonguay, P., 2012. High-order energy stable flux reconstruction schemes for fluid flow simulations on unstructured grids. Ph.D. thesis, STANFORD.

[3] Castonguay, P., Vincent, P. E., Jameson, A., Apr. 2012. A new class of high-order energy stable flux reconstruction schemes for triangular elements. J. Sci. Comput. 51 (1), 224–256.

[4] Castro-Diaz, M. J., Hecht, F., Mohammadi, B., Pironneau, O., 1997. Anisotropic unstructured mesh adaption for flow simulations. International Journal for Numerical Methods in Fluids 25 (4), 475–491.

[5] Dompierre, J., Vallet, M.-G., Bourgault, Y., Fortin, M., Habashi, W. G., 2002. Anisotropic mesh adaptation: towards user-independent, mesh-independent and solver-independent CFD. part III. unstructured meshes. International Journal for Numerical Methods in Fluids 39 (8), 675–702.

[6] Ekaterinaris, J., 2005. High-order accurate, low numerical diffusion methods for aerodynamics. Progress in Aerospace Sciences 41 (3-4), 192–300.

[7] Fidkowski, K., 2011. Review of output-based error estimation and mesh adaptation in computational fluid dynamics. AIAA Journal 49 (4), 673–694.

[8] Fidkowski, K., Darmofal, D., 2007. A triangular cut-cell adaptive method for high-order discretizations of the compressible Navier-Stokes equations. Journal of Computational Physics 225 (2), 1653–1672.

[9] Fidkowski, K., Roe, P., 2009. Entropy-based mesh refinement, I: The entropy adjoint approach.

[10] Fidkowski, K., Roe, P., 2010. An entropy adjoint approach to mesh refinement. SIAM Journal on Scientific Computing 32 (3), 1261–1287.

[11] Gao, H., Wang, Z. J., 2011. A residual-based procedure for hp-adaptation on 2D hybrid meshes. AIAA Paper 2011-492.

[12] Gao, H., Wang, Z. J., Jan. 2013. A conservative correction procedure via reconstruction formulation with the chain-rule divergence evaluation. Journal of Computational Physics 232, 7–13.

[13] Gao, H., Wang, Z. J., 2013. Differential formulation of discontinuous Galerkin and related methods for the Navier-Stokes equations. Commun. Comput. Phys. 13, 1013–1044.

[14] Hartmann, R., Houston, P., 2002. Adaptive discontinuous Galerkin finite element methods for the compressible Euler equations. Journal of Computational Physics 183 (2), 508 – 532.

[15] Hesthaven, J., Warburton, T., 2008. Nodal Discontinuous Galerkin Methods: Algorithms, Analysis and Applications. Vol. 54. Springer-Verlag New York Inc.

[16] Huang, W., Russell, R. D., 2010. Adaptive Moving Mesh Methods. Vol. 174. Springer.

[17] Huynh, H. T., 2007. A flux reconstruction approach to high-order schemes including discontinuous Galerkin methods. AIAA Paper 2007-4079.

[18] Huynh, H. T., 2009. A reconstruction approach to high-order schemes including discontinuous Galerkin for diffusion. AIAA Paper 2009-403.

[19] Huynh, H. T., 2011. High-order methods by correction procedures using reconstructions. Adaptive High-Order Methods in Computational Fluid Dynamics 2, 391–422.

[20] Jameson, A., Vincent, P. E., Castonguay, P., Feb. 2012. On the non-linear stability of flux reconstruction schemes. J. Sci. Comput. 50 (2), 434–445.

[21] Karniadakis, G., Sherwin, S., 1999. Spectral/hp Element Methods for CFD. Oxford University Press, USA.

[22] Kopriva, D., Kolias, J., 1996. A conservative staggered-grid chebyshev multidomain method for compressible flows. Journal of computational physics 125 (1), 244–261.

[23] Kopriva, D. A., 1996. A conservative staggered-grid chebyshev multidomain method for compressible flows. II. a semi-structured method. Journal of Computational Physics 128 (2), 475 – 488.

[24] Liang, C., Cox, C., Plesniak, M., 2013. A comparison of computational efficiencies of spectral difference method and correction procedure via reconstruction. Journal of Computational Physics 239 (0), 138 – 146.

[25] Liang, C., Jameson, A., Wang, Z. J., May 2009. Spectral difference method for compressible flow on unstructured grids with mixed elements. Journal of Computational Physics 228 (8), 2847–2858.

[26] Liu, Y., Vinokur, M., Wang, Z. J., 2006. Spectral finite volume method for conservation laws on unstructured grids V: Extension to three-dimensional systems. Journal of Computational Physics 212 (2), 454–472.

[27] Lohner, R., Morgan, K., Peraire, J., Vahdati, M., 1987. Finite element flux-corrected transport for the Euler and Navier-Stokes equations. International Journal for Numerical Methods in Fluids 7 (10), 1093–1109.

[28] May, G., Jameson, A., 2006. A spectral difference method for the Euler and Navier-Stokes equations on unstructured meshes. AIAA paper 2006-304.

[29] Shi, L., Wang, Z. J., 2015. Adjoint-based Error Estimation and Mesh Adaptation for the Correction Procedure via Reconstruction Method. Journal of Computational Physics 295, 261–284.

[30] Shi, L., Wang, Z. J., Zhang, L., Liu, W., Fu, S., 2014. A PNPM-CPR framework for hyperbolic conservation laws. Journal of Scientific Computing, 1–27.

[31] Shu, C.-W., 1997. Essentially non-oscillatory and weighted essentially non-oscillatory schemes for hyperbolic conservation laws. Tech. rep.

[32] T. Haga, H. G., Wang, Z. J., 2011. A high-order unifying discontinuous formulation for the Navier-Stokes equations on 3D mixed grids. Math. Model. Nat. Phenom. 6 (03), 28–56.

[33] Taneda, S., Oct. 1956. Experimental Investigation of the Wake behind a Sphere at Low Reynolds Numbers. Journal of the Physical Society of Japan 11, 1104.

[34] Van den Abeele, K., Lacor, C., Wang, Z. J., 2008. On the stability and accuracy of the spectral difference method. Journal of Scientific Computing 37 (2), 162–188.

[35] Venditti, D., Darmofal, D., 2003. Anisotropic grid adaptation for functional outputs: application to two-dimensional viscous flows. Journal of Computational Physics 187 (1), 22–46.

[36] Venditti, D. A., Darmofal, D. L., Oct. 2000. Adjoint error estimation and grid adaptation for functional outputs: application to quasi-one-dimensional flow. Journal of Computational Physics 164 (1), 204–227.

[37] Wang, L., Mavriplis, D. J., Nov. 2009. Adjoint-based hp-adaptive discontinuous Galerkin methods for the 2D compressible Euler equations. Journal of Computational Physics 228 (20), 7643–7661.

[38] Wang, Z. J., 2002. Spectral (finite) volume method for conservation laws on unstructured grids: basic formulation. Journal of Computational Physics 178 (1), 210–251.

[39] Wang, Z. J., 2007. High-order methods for the Euler and Navier-Stokes equations on unstructured grids. Progress in Aerospace Sciences 43 (1-3), 1–41.

[40] Wang, Z. J., May 2011. Adaptive High-Order Methods in Computational Fluid Dynamics. World Scientific Publishing.

[41] Wang, Z. J., Fidkowski, K., Abgrall, R., Bassi, F., Caraeni, D., Cary, A., Deconinck, H., Hartmann, R., Hillewaert, K., Huynh, H. T., Kroll, N., May, G., Persson, P.-O., van Leer, B., Visbal, M., Jul. 2013. High-order CFD Methods: Current Status and Perspective. International Journal for Numerical Methods in Fluids 72, 811–845.

[42] Wang, Z. J., Gao, H., 2009. A unifying lifting collocation penalty formulation including the discontinuous Galerkin, spectral volume/difference methods for conservation laws on mixed grids. Journal of Computational Physics 228, 8161–8186.

[43] Wang, Z. J., Gao, H., Haga, T., 2011. A unifying discontinuous formulation for hybrid meshes. Adaptive High-Order Methods in Computational Fluid Dynamics, 423–453.

[44] Wang, Z. J., Liu, Y., 2002. Spectral (finite) volume method for conservation laws on unstructured grids II. extension to two-dimensional scalar equation. Journal of Computational Physics 179 (2), 665–697.

[45] Yang, X., Huang, W., Qiu, J., 2012. A moving mesh weno method for one-dimensional conservation laws. SIAM Journal on Scientific Computing 34 (4), A2317–A2343.